Mean Field Annealing Deformable Contour Method: A Constrained Global Optimization Approach

Abstract

This paper presents an efficient constrained global optimization approach based on mean field annealing (MFA) theory to the problem of contour energy minimization with a contour interior constraint for object boundary extractions. In the method, with a given contour energy function, different target boundaries can be modeled as constrained global optimal solutions under different constraints expressed as a set of parameters characterizing the target contour interior structures. To search for the constrained global optimal solutions, a fast and efficient global approach based on MFA is employed to avoid local minima, which has been very difficult to achieve in most deformable contour methods. As an illustrative example, three target boundaries in a synthetic image are modeled as constrained global energy minimum contours with different constraint parameters and are successfully located using the derived algorithm. A conventional variational based deformable contour method [1] with the same energy function and constraint fails to achieve the same task. Experimental evaluations and comparisons with other methods on ultrasound pig heart, MRI knee, and CT kidney images where gaps, blur contour segments having complex shape and inhomogeneous interiors have been conducted with most favorable results.

Keywords: Snakes, curve evolution, variational based approach, level set, and mean field annealing.

1. Introductions

Image segmentation is a fundamental issue in computer vision. Energy based approach [22] [23] [2] may be one of the most influential image segmentation approaches. The basic idea of energy based methods is to model some global image properties [22] that capture the characteristics of the target regions/boundaries into energy functions; and then retrieve these target regions/boundaries via an energy minimization process. There are two important factors in most energy based methods: energy function formulations and energy minimization approaches. Energy functions may be classified as image based energy functions [22], for segmenting an entire image, and contour/region based energy, for object segmentations [2] [4]. Given an energy formulation, energy minimization approaches are then to minimize energy for retrieving the desired energy minimum. Generally, most energy minimization approaches are local methods [2] [4]. Since local energy minima can be arbitrarily far from the global optimum, these approaches may produce results that may not convey any of the global image properties encoded in energy functions. Some global approaches including simulated annealing [23] [14] [15], graph theory [22], and deterministic annealing [21] have also been proposed with rather successful results. Simulated annealing approaches often demand a high computational complexity [23] [14]. To reduce the computational complexity, faster temperature parameter decreasing scheme are used but may produce local energy minimum solutions that may be far from the global optimal solutions [24]. Graph theory based image segmentation methods provide a more efficient global approach for some energy functions [22]. Most of these methods [22] are used for image classification and are difficult in incorporating object shape information [25]. Deterministic annealing [26] has been successfully applied for data clustering problems and is further extended for texture image classification applications [21].

In this paper, we apply mean field annealing approach (MFA), which is a deterministic annealing approach and requires much less computational complexity than simulated annealing, to a problem of global energy minimization under a region constraint for object boundary extraction. In the method, with a given contour energy function, different target boundaries can be modeled as constrained global optimal solutions under different constraints expressed as a set of parameters characterizing the target contour interior structure. To search for the constrained global optimal solutions, the method takes a Lagrange approach and then introduces a quadratic constraint based on the square error of the current parameter values and the optimal values to convexify the Lagrange multiplier function [29]. The proposed method considers the deformable contour and the associated variables as random functions or variables in the convexified Lagrange multiplier; and then incorporates variational based deformable contour searching into MFA framework using saddle point approximation and combines it with an MFA parameter optimization scheme. High computational complexity is thus avoided. Notice that the mean field approximation used in [17] is not the same as the mean field annealing used in this formulation to achieve a global optimal solution.

In Section 2, related works on deformable contour methods are reviewed. In Section 3 and 4, MFA theory and the problem formulation are introduced and discussed. Section 5 details the derivation of the proposed approach. Illustrative examples and parameter setting experiments are shown in Section 6 and Section 7 respectively, while applications on biomedical images are demonstrated in Section 8. In section 9, the conclusion regarding this method is provided.

2. Related works

Deformable contour methods (DCMs), since originated by Kass et al [2], receive tremendous amount of attentions, and many efforts have been made to apply them to all sorts of problems. Typically, most DCMs [2] [4] [12] [13] model boundary extractions as energy minimization problems. Traditionally these methods often use functions of image gradient [2] [4] as contour energies. In cases where image gradient information is either noisy or inaccurate in identifying target boundary, the image gradient based energy functions often have multiple energy minima and as a result, these methods often result in undesired local energy minimum contour instead of target boundary. To deal with this problem, improvements in DCMs can be divided into two categories.

In the first category, the methods [1] [5] [6] [7] [8] [16] propose new energy functions integrating region based image features to alleviate the problem of multiple energy minima. In [6] [7], region based energy functions firstly introduced in image classification methods are used to derive the deformable contour formulations and in [8] theses functions are further combined with the image gradient based contour energy functions to improve the performances. In general, the above methods are rather robust to noises and the segmentation is efficiency is improved [16]. However, in more challenging situations, in which a combination of region and image gradient information still can not accurately identify the target boundary (such as gaps and inhomogeneous interiors all present in one contour extraction problem), the methods still often result in undesired local energy minima; for instance, the resulting contours may either expand beyond the gaps or stops at noisy interiors. One way to handle the problem is to integrate priori shape model into the frameworks [18] [19] [20] to assist identifying target boundary. The problem with these methods is that a reliable shape model construction often requires intensive manual interventions.

The second category of DCMs model target boundary as global energy minimum [14] [15] and take global optimization approaches, mostly simulated annealing, to locate them. These methods are robust to undesired local energy minima. However, in a complex image context, with a snake based contour energy function, the target boundary is usually a global energy minimum under certain constraints (for instance, the constraints of the contour interior characteristics) instead of the actual global energy minimum contour throughout the entire image. Thus in [14] [15], either a major modification of the energy function, incorporating specific prior knowledge on target boundary [14] to make it be the global energy minimum contour, or a preset mask [15] constraining the contour searching space within a neighborhood close to target boundary is often required.

3. A Brief Review of Mean Field Annealing

Mean field annealing is a global optimization method derived from statistical mechanics [9]. Let f be a random variable and $E(f)$ be an energy function to be minimized. Without any prior knowledge, the probability distribution of f is assumed to be Gibbs distribution,

$$P(f) = \frac{1}{Z}\exp\left(-\frac{1}{T}E(f)\right) \tag{1}$$

with the partition function Z being

$$Z = \sum_{f \in P^*} \exp\left(-\frac{1}{T}E(f)\right) \tag{2}$$

where P^* is all the possible configurations of f and T is the temperature. The statistical mean of f at temperature T is defined as,

$$\overline{f(T)} = \sum_{f \in P^*} fP(f) = \sum_{f \in P^*} f\frac{1}{Z}\exp\left(-\frac{1}{T}E(f)\right) \tag{3}$$

According to mean field annealing theory [9], $\overline{f(T)}$ is of importance due to the well known fact that as the temperature approaches zero, $\overline{f(T)}$ approaches the global optimal point f^*,

$$\lim_{T\to 0}\overline{f(T)} = \lim_{T\to 0}\sum_{f\in P^*} fP(f) = f^* \tag{4}$$

This suggests that instead of minimizing $E(f)$ directly, we can try to evaluate mean field $\overline{f(T)}$ and then track $\overline{f(T)}$ from a sufficiently high temperature down to zero. The value of $\lim_{T\to 0}\overline{f(T)}$ is then the global optimal point.

In applications, $\overline{f(T)}$ can be evaluated using saddle point approximation theorem [9]. The theorem states that at temperature T, the partition function Z can be approximated by

$$Z \approx M\exp\left(-\frac{1}{T}E(\overline{f(T)})\right)$$

where M is a constant and $E(\overline{f(T)})$ satisfies $\left.\frac{\partial E(f)}{\partial f}\right|_{f=\overline{f(T)}} = 0$.

Note that in many applications, f is a random function of time t rather than a random variable. In these cases, the mean of f at temperature T is also a function of t.

4. Problem Formulation

Problem statement

Let Φ be an open domain subset of $\Re^2$ and $I(x,y):\Phi \to \Re$ be the image intensity function. Consider a target object with boundary $\Gamma(q)$ and interior Ω_Γ in the image. The average image intensity in Ω_Γ, I_0, and the variance of image intensity in Ω_Γ, s^2, can be determined as

$$I_0 = \frac{\iint_{\Omega_\Gamma} I(x,y)dxdy}{\iint_{\Omega_\Gamma} dxdy},$$

and

$$s^2 = \frac{\iint_{\Omega_\Gamma} \left(I(x,y) - I_0\right)^2 dxdy}{\iint_{\Omega_\Gamma} dxdy},$$

We can model target boundary $\Gamma(q)$ as a close contour having the global minimum energy,

$$E_C(\Gamma(q)) = \oint_{\Gamma(q)} g(|\nabla I(\Gamma(q))|)ds \tag{5}$$

satisfying

$$D(x,y) \geq T_V \quad \text{if } (x,y) \in \Omega_\Gamma \tag{6}$$

where s is the normalized arc length**,** q is the contour parameter. $g(|\nabla I(\Gamma(q))|)$ is a contour energy function firstly introduced in [4], which can be any positive decreasing function. In the paper, we choose

$$g(|\nabla I(\Gamma(q))|) = \frac{1}{1 + |\nabla I(\Gamma(q))|^2} + a, \tag{7}$$

$\nabla I(\Gamma(q))$ is the gradient of $I(x,y)$ with (x,y) on $\Gamma(q)$, $a > 0$ is a constant. As we can see from Eq. (7), when $\nabla I(\Gamma(q))$ is large, $g(|\nabla I(\Gamma(q))|)$ approaches its minimum a; when $\nabla I(\Gamma(q))$ approaches zero, $g(|\nabla I(\Gamma(q))|)$ approaches its maximum a + 1. a is related to contour smoothness. A large a indicates a smooth contour while a small a indicates just the opposite.

$D(x,y)$, which is used to characterize Ω_Γ, is a function of I_0 and s^2. In the paper, we choose

$$D(x,y) = \exp\left[-\frac{(I(x,y)-I_0)^2}{b s^2}\right], \tag{8}$$

where b is a positive constant set as 2.0. $T_V > 0$ is a threshold that can be adjusted for modeling different target boundaries as constrained global energy minima. A large T_V often indicates a small admissible set of contours that satisfy the constraint of Eq. (6) while a small T_V indicates just the opposite.

Then our problem is to estimate the optimal values of s^2, I_0 and then find a close contour $C(q, t)$ enclosing region $\Omega_c(t)$ at time t, such that

$$E_C(C(q,t)) = \oint_C g(|\nabla I(C(q,t))|)ds \tag{9}$$

is the global minimum under the constraint,

$$D(x,y) \geq T_V \quad \text{for } (x,y) \in \Omega_C(t) \tag{10}$$

The Lagrange formulation of Eq. (9) is

$$L(C(q,t), s^2, I_0) = \oint_C g(|\nabla I(C(q))|)ds - l_1 \iint_{\Omega_C} (D(x,y) - T_V)dxdy \tag{11}$$

where $l_1 > 0$ is a Lagrange multiplier. Since $\Gamma(q)$ is the constrained global energy minimum, according to Lagrange multiplier condition, the optimal setting of l_1, l_1^*, should satisfy

$$\left.\frac{\partial L(C(q,t), s^2, I_0, l_1)}{\partial C(q,t)}\right|_{\substack{C(q,t)=\Gamma(q) \\ l_1 = l_1^*}} = 0 \tag{12}$$

According to [1],

$$\frac{\partial L(C(q,t), s^2, I_0, l_1)}{\partial C(q,t)} \propto F(C(q,t), s^2, I_0, l_1) = l_1\left[D(x(q,t), y(q,t)) - T_V\right] + kg(|\nabla I(C(q,t))|) - \nabla g(|\nabla I(C(q,t))|) \cdot \vec{N}$$

where k is contour curvature and $\vec{N}$ is the normal direction of $C(q, t)$. Thus satisfying Eq. (12) is equivalent to satisfying

$$F(\Gamma(q), s^2, I_0, l_1^*) = 0 \tag{13}$$

In implementations, it may be difficult to find a l_1^* satisfying Eq. (13). As an alternative, we search for a l_1^* such that

$$\left\| F(\Gamma(q), s^2, I_0, l_1^*) \right\|_m = \min \left\| F(\Gamma(q), s^2, I_0, l_1) \right\|_m \qquad \text{for } l_1 \in \Re \tag{14}$$

where $\|a\|_m$ is the m norm function of a and $m > 0$. To simplify the computation of Eq. (14), we often choose m as ∞, and l_1^* can then be determined. With this, Eq. (11) can be finally written as

$$L(C(q,t), s^2, I_0, l_1^*) = \oint_C g(|\nabla I(C(q,t))|)ds - l_1^* \iint_{\Omega_C} (D(x,y) - T_V)dxdy \tag{15}$$

A brief review of the original constrained optimization approach [1] [16] and its limitations

To minimize Eq. (15), the original constrained optimization deformable contour method (CODCM) [1] initially estimates s^2, I_0, l_1^* and then minimizes $L(C(q,t), s^2, I_0, l_1^*)$ using a variational approach. The contour evolution formula is

$$\frac{\partial C(q,t)}{\partial t} = \left\{ l_1^* \left[D(x,y) - T_V \right] + kg(|\nabla I|) - \nabla g \cdot \vec{N} \right\} \vec{N} \tag{16}$$

Since $\oint_C g(|\nabla I(C(q,t))|)ds$ is nonconvex having multiple local energy minima and l_1^* is often small, Eq. (16) tends to be trapped into local energy minima. An extra constant balloon force b has to be added,

$$\frac{\partial C(q,t)}{\partial t} = \left\{ (l_1^* + b) \left[D(x,y) - T_V \right] + kg(|\nabla I|) - \nabla g \cdot \vec{N} \right\} \vec{N} \tag{17}$$

The added balloon force b can be viewed as to increase the weight of the region constraint. The difficulty with Eq. (17) is that with a small b, $L(C(q,t), s^2, I_0, l_1^*)$ is still nonconvex and has multiple minima while with a large b, locating the global minimum of $L(C(q,t), s^2, I_0, l_1^*)$ is equivalent to locating a local energy minimum near the maximum of $\iint_{\Omega_C} (D(x,y) - T_V)dxdy$, which is not necessarily the constrained global energy minimum. Though CODCM is rather successful in many applications [16], in more challenging situations, in which gaps and inhomogeneous interiors are all present in a single contour extraction problem, the methods may still either expand beyond the gaps (with a large *b*) or stops at the noisy interiors (with a small *b*).

Another problem is that when some a priori information about the target object is unavailable, an accurate estimation of s^2, I_0, and l_1^* is often difficult especially when the object interior is inhomogeneous as shown in Fig. 6.1a; In [1], I_0 is computed as the mean brightness of the deforming contour and is updated during the contour deformation. Since l_1^* is small, $l_1^* + b$ can be approximated by the constant *b*. s^2 is the only parameter needs tuning.

5. The Derivation of the Approach

Energy function formulation

To overcome the difficulties of CODCM [1] [16], we add an extra constraint $E_p - T_p \leq 0$ that can convexify Eq. (15) without deviating the global optimal solutions,

where
$$E_p = (s^2 - s_C^2)^2 + (I_0 - I_0^C)^2 + (l_1^* - l_1^C)^2 \tag{18}$$

$T_p \geq 0$ is a small constant. s_C^2, I_0^C, and l_1^C are obtained from $\Omega_C(t)$ as follows:

$$I_0^C = \frac{\iint_{\Omega_C} I(x,y)dxdy}{\iint_{\Omega_C} dxdy}, \tag{19}$$

$$s_C^2 = \frac{\iint_{\Omega_C} [I(x,y) - I_0]^2 dxdy}{\iint_{\Omega_C} dxdy}, \tag{20}$$

$$\left\|F(C(q,t), s^2, I_0, l_1^C)\right\|_m = \min \left\|F(C(q,t), s^2, I_0, l_1)\right\|_m \tag{21}$$

Then Eq. (15) can be written as,

$$L_p(C(q,t), s^2, I_0, l_1^*) = \overbrace{\oint_C g(|\nabla I(C(q))|)ds - l_1^* \iint_{\Omega_C} (D(x,y) - T_V)dxdy}^{E_I} + \overbrace{l_2(E_p - T_p)}^{E_{II}} \tag{22}$$

where $l_2 > 0$ is another Lagrange multiplier. E_{II} is a convex quadratic function [29] with the global minimum at $\Gamma(q)$. With the introduction of E_{II} and a large $l_2 >> l_1^*$, $L_p(C(q,t), s^2, I_0, l_1^*)$ is convexified with the global minimum at target boundary $\Gamma(q)$. The introduction of E_{II} is to require that the associated parameters of the resulting contour closed to those of target boundary $\Gamma(q)$. We can take a derivative based approach to minimize Eq. (22), which produces alternating procedures of contour evolution (computed according to Eq. (16)) and the updating of s^2, I_0, and l_1^* (by letting $s^2 = s_C^2$, $I_0 = I_0^C$, and $l_1^* = l_1^C$). The problem is that the approach is a local method and often fails to locate global energy minimum.

The derivations of the proposed approach

To find the global optimal solution, we apply the framework of MFA discussed in Section 3 to minimize Eq. (22). Consider $C(q,t)$ as a random function of time t and parameters s^2, I_0, and l_1^* as random variables. Consider a proper temperature sequence T_i, $1 \le i \le n$, satisfying $T_{i+1} < T_i$, $T_n = 0$. According to MFA approach, $C(q,t)$, s^2, I_0, and l_1^* can be regarded as all random functions of temperature T_i. Thus we denote $C(q,t)$, s^2, I_0, and l_1^* as $C(q,t,T_i)$, $s^2(T_i)$, $I_0(T_i)$, $l_1^*(T_i)$. Our strategy to search for the global optimum of $C(q,t)$, s^2, I_0, and l_1^* is to track the mean values of $C(q,t,T_i)$, $s^2(T_i)$, $I_0(T_i)$, and $l_1^*(T_i)$ until T_i drops to zero as i goes from 1 to n. To estimate the mean values of $C(q,t,T_i)$, $s^2(T_i)$, $I_0(T_i)$, and $l_1^*(T_i)$, according to [9], we can ignore the correlations of the mean field of $C(q,t,T_i)$, $s^2(T_i)$, $I_0(T_i)$, $l_1^*(T_i)$ and proceed to update each variables separately by holding all other parameters unchanged. Let $C(q,0,T_1)$ be the given initial contour denoted as $C(T_1)$. Let $s_{in}^2(T_1) = s_{C(T_1)}^2$, $I_0^{in}(T_1) = I_0^{C(T_1)}$, and $l_1^{in}(T_1) = l_1^{C(T_1)}$. Let $i=1$ and go to Step 1.

Step1 is to keep $s^2(T_i) = s_{in}^2(T_i)$, $I_0(T_i) = I_0^{in}(T_i)$, $l_1^*(T_i) = l_1^{in}(T_i)$ constant and compute the mean value of $C(q,t,T_i)$. By MFA theory discussed in Section 3, the mean of $C(q,t,T_i)$ can be evaluated from partition function using the saddle point approximation. At temperature T_i, the partition function Z can be approximated by

$$Z \approx M \exp\left(-\frac{1}{T_i} L_p(\overline{C(q,t,T_i)}, s^2(T_i), I_0(T_i), l_1^*(T_i))\right),$$

where $\left.\frac{\partial L_p(C(q,t), s^2(T_i), I_0(T_i), l_1^*(T_i))}{\partial C(q,t)}\right|_{C(q,t)=\overline{C(q,t,T_i)}} = 0$. In applications, the variations of l_1^C, s_C^2, and I_0^C are much slower comparing to that of $C(q,t)$ therefore we neglect their fluctuations during the deformation of $C(q,t)$. With this, according to [1], $\overline{C(q,t,T_i)}$ can then be computed by letting,

$$\left.\frac{\partial C(q,t)}{\partial t}\right|_{\substack{C(q,t)=\overline{C(q,t,T_i)} \\ C(q,0)=C(T_i)}} = \left.\frac{\partial L_p(C(q,t), s^2(T_i), I_0(T_i), l_1^*(T_i))}{\partial C(q,t)}\right|_{C(q,t)=\overline{C(q,t,T_i)}} = 0 \qquad (23)$$

where
$$\frac{\partial C(q,t)}{\partial t} = \left\{l_1^*(T_i)\left[D(x,y,T_i) - T_V\right] + kg(|\nabla I|) - \nabla g \cdot \vec{N}\right\}\vec{N} \qquad (24)$$

and
$$D(x,y,T_i) = \frac{(I(x,y) - I_0(T_i))^2}{b s^2(T_i)}.$$

To implement constraint of Eq. (23), we relax it as

$$\left.\frac{\partial C(q,t)}{\partial t}\right|_{\substack{C(q,t)=\overline{C(q,t,T_i)} \\ C(q,0)=C(T_i)}} \leq T_C \qquad (25)$$

where $T_C \geq 0$ is a given constant. To reduce computational complexity, instead of satisfying Eq. (23), contour $C(q,t)$ is deformed for a certain time interval $l > 0$ and we assume that Eq. (25) can be satisfied after the interval. Then $\overline{C(q,t,T_i)}$ can be computed according to Eq. (24) by letting $\overline{C(q,t,T_i)} = C(q,l)$ with $C(q,0) = C(T_i)$ being the initial contour.

Step2 is to keep $\overline{C(q,t,T_i)}$ constant and calculate $s^2(T_i)$, $I_0(T_i)$, $l_1^*(T_i)$. We denote the mean values of $s^2(T_i)$, $I_0(T_i)$, $l_1^*(T_i)$ as $\overline{s^2(T_i)}$, $\overline{I_0(T_i)}$, $\overline{l_1^*(T_i)}$ and $s_C^2(T_i)$, $I_0^C(T_i)$, $l_1^C(T_i)$ as values of s_C^2, I_0^C, and l_1^C computed from $\overline{C(q,t,T_i)}$, respectively. With the derivation given in the Appendix, we have

$$\overline{I_0(T_i)} = I_0^C(T_i), \qquad (26)$$

$$\overline{s^2(T_i)} = s_C^2(T_i) + \sqrt{\frac{T_i}{p}}, \tag{27}$$

and

$$\overline{l_1^*(T_i)} = l_1^C(T_i) + \sqrt{\frac{T_i}{p}} \tag{28}$$

Then let $I_0^{in}(T_{i+1}) = \overline{I_0(T_i)}$, $s_{in}^2(T_{i+1}) = \overline{s^2(T_i)}$, $l_1^{in}(T_{i+1}) = \overline{l_1^*(T_i)}$, $C(T_{i+1}) = \overline{C(q,t,T_i)}$. (29)

Let $i = i+1$ and go to Step1 until temperature drops to zero.

Comments:

The above solution includes two alternative procedures of contour deformation of Eq. (24) and parameter updating of Eq. (26) to (28). Eq. (24) is similar to Eq. (16) of CODCM [1]. However, in Eq. (24), the values of $s^2(T_i)$, $I_0(T_i)$, and $l_1^*(T_i)$ vary during the contour deformation as shown in Eq. (26) to Eq. (28). From Eq. (27), it is easy to see that $s^2(T_i)$ is large when temperature is high and $s^2(T_i)$ gradually reduces when the temperature lowers as the contour grow outward. The value of temperature T_i controls the dynamic range of $s^2(T_i)$ thus determines the method's adaptability to the inhomogeneous interiors and noises. It is also interesting to note that according to Eq. (28) the magnitude of the balloon force velocity term in Eq. (24) is decaying during the contour evolution process. This feature provides the method more robustness to noisy interiors while enhancing its performances in situations of gaps and blur boundaries. In general, the whole contour deformation process can be viewed as an annealing process, in which contour flows outward in a high temperature and then cools down and anneals near the target boundary.

Algorithm description

From the above discussions, an iterative algorithm can be derived as follows:

For an initial contour $C(q,t)$ with the size of 5 by 5, $t=0$ and interior $\Omega_C(t)$, at temperature $T_i = T_{init}$ $i=1$, where T_{init} is the initial temperature, let $\overline{C(q,t,T_i)} = C(q,t)$ do

i) Compute s_C^2, I_0^C, and l_1^C from $\overline{C(q,t,T_i)}$ using Eq. (19), Eq. (20), and Eq. (21).

ii) Update $\overline{s^2(T_i)}$, $\overline{I_0(T_i)}$, and $\overline{l_1^*(T_i)}$ using Eq. (26), Eq. (27), and Eq. (28).

iii) Let $T_{i+1} = T_i * decT$, and update $s_{in}^2(T_i)$, $I_0^{in}(T_i)$, $l_1^{in}(T_i)$, and $C(T_i)$ according to Eq. (29), where $0 < decT < 1$ is the updating factor.

iv) Evolve $C(q,t)$ for l iterations ($l > 0$ is a constant) according to Eq. (24) using narrow band numerical scheme [3] with $C(q,0) = C(T_i)$ being the initial contour. Let $\overline{C(q,t,T_i)} = C(q,l)$. Stop when the maximum velocity of $C(q,l)$ is smaller than a threshold V_t or a maximum iteration number t_m has been reached, where V_t and t_m are positive constants. To further increase the robustness of the algorithm to the setting of iteration number t_m, we compute the value of contour energy according to Eq. (9) and record the lowest energy contour. The output contour is then the contour with lowest contour energy.

It should be noted that we can also set the stopping criteria as when the temperature T_i drops to zero. However, this stopping criterion is too sensitive to the settings of T_{init} and $decT$ thus is not used.

Some remarks on Appendix:

As illustrated in Appendix, if $\overline{\Omega_C(t,T_1)} \subseteq \Omega_\Gamma$, where $\overline{\Omega_C(t,T_1)}$ is the interior of $\overline{C(q,t,T_1)}$ and Ω_Γ is the interior of target boundary, there exists at least one temperature sequence T_i, $1 \le i \le n$ such that $\overline{C(q,t,T_i)}$ computed according to Eq. (24) and Eq. (26) to (28) satisfies $\overline{\Omega_C(t,T_i)} \subseteq \Omega_\Gamma$. In applications, we assume that $\overline{\Omega_C(t,T_i)} \subseteq \Omega_\Gamma$ can be satisfied by a careful selection of T_{init} and $decT$. Tuning T_{init} and $decT$ are thus needed in some applications. As an advantage, with the satisfaction of $\overline{\Omega_C(t,T_i)} \subseteq \Omega_\Gamma$, the method can be applied to extract any target boundary $\Gamma(q)$ that can be modeled as the global energy minimum contour with the constraint $\Omega_C^{in} \subseteq \Omega_\Gamma$, where Ω_C^{in} is the interior of an arbitrary contour inside Ω_Γ, as shown in Fig. 8.4 and 8.5. In the viewpoint of global optimization, the physical meaning of the solutions Eq. (24) and (26) to (28) is that since $\overline{\Omega_C(t,T_i)} \subseteq \Omega_\Gamma$ is satisfied and the contour is mainly moving outward, when i approaches n, $\overline{C(q,t,T_i)}$ is more closed to the target boundary and $s_C^2(T_i)$, $I_0^C(T_i)$, $I_1^C(T_i)$ are more close to s^2, I_0, and I_1^*.

6. Illustrative Examples

In this section, we will show that different target boundaries in a single image can be modeled as the constrained global minima with different settings of T_V. We then illustrate the processes of locating these constrained global energy minima using the proposed method with a comparison to the results using Eq. (17) of CODCM [1] assuming that s^2 and I_0 of the target objects are known.

The examples shown in Fig. 6.1(a) is a 165 by 165 image designed with three overlapping circles MC_1, MC_2, MC_3 of size $r_1 = 40$ pixels (MC_1), $r_2 = 55$ pixels (MC_2), $r_3 = 70$ pixels (MC_3) at different center locations, where r_i, $i = 1,2,3$ is the radius of circle MC_i. The interior brightness of circles MC_1 and MC_3 is radially decreasing from the centers to their perimeters in a straight line fashion for circle MC_1 from 255 to 207, circle MC_3 from 160 to 69 with the scale of 255 gray levels while the interior brightness of MC_2 is radially increasing from the center to the perimeter in a straight line fashion from 40 to 150. The values of s^2, I_0, and $D_{\min}(x,y)$ inside MC_1, MC_2, MC_3, and the respective contour energy E_C (computed according to Eq. (9)) are listed in the Table 6.1, where $D_{\min}(x,y)$ is the minimum of $D(x, y)$,

	$D_{\min}(x,y)$	s^2	I_0	E_C
MC_1	0.016	127.7	223	0.00383
MC_2	0.289	2359	178	0.00547
MC_3	0.174	3682	142	0.00411

Table 6.1 The parameters and contour energy for MC_1, MC_2, and MC_3

It is easy to see that when T_V is set smaller than 0.016, the value of $D_{\min}(x,y)$ inside MC_1, MC_1 is the constrained global energy minimum. When T_V is larger than 0.016 but smaller than $D_{\min}(x,y)$ inside MC_3, 0.174, the constrained global energy minimum is MC_3. When T_V is larger than 0.174 but smaller than $D_{\min}(x,y)$ inside MC_2, 0.289, MC_2 becomes the constrained global energy minimum. Thus MC_1,

MC_2, MC_3 can all be modeled as the constrained global energy minimum by setting different values of T_V, respectively $T_V = 0.01$ for MC_1, $T_V = 0.1$ for MC_3, $T_V = 0.25$ for MC_3. The extraction processes of MC_1, MC_2, MC_3 are shown in Fig. 6.1b to 6.1e, 6.2a to 6.2e, and 6.3a to 6.3e. With the same initial contour position indicated as the black dot in Fig. 6.1a, the method successfully locates all the constrained global energy minimum contours. In the experiments, we set $decT$ as 0.966 and respectively set $T_{init} = 10^6$ for MC_1, $T_{init} = 10^8$ for MC_2, and $T_{init} = 10^{11}$ for MC_3. The results of [1] using the same initial contour in Fig. 6.1a and Eq. (17) by assuming that I_0 and s^2 of MC_1, MC_2, and MC_3 are known (as listed in Table 6.1) are shown in Fig. 6.4b to 4e, 5a to 5e, and 6a to 6e. Though Eq. (17) successfully extracts MC_1, it fails to extract MC_2 and MC_3. To illustrate the key differences between the behaviors of the two methods, Fig. 6.7a to 6.7e show the scaled images of $D(x,y,T_i) - T_V = \dfrac{(I(x,y) - I_0(T_i))^2}{b s^2(T_i)} - T_V$ in Eq. (24) under the temperatures respectively corresponding to Fig. 6.3a to 6.3e; and Fig. 6.8a show the scaled image of $D(x,y) - T_V = \dfrac{(I(x,y) - I_0^{MC_3})^2}{b s^2_{MC_3}}$ in Eq. (17), where $I_0^{MC_3}$ and $s^2_{MC_3}$ are the mean brightness and variance of image intensity inside MC_3. We note that in Fig. 6.7a and 6.7b the variations of $D(x,y,T_i) - T_V$ are small and the fluctuations of the brightness distributions across MC_1, MC_2, and MC_3 are only mildly reflected in contour velocity. Therefore it is easy for the contour to overcome the inhomogeneous interiors of MC_3. From 6.7c to 6.7e, the variations of $D(x,y,T_i) - T_V$ become larger and the steep fluctuations of the brightness distributions across MC_1, MC_2, MC_3 becomes more evidently reflected in contour velocity. Noting that the contour has already marched over most sections of MC_1, MC_2 and has been closed to MC_3 as shown in Fig. 6.3c to 6.3e, the steep variations of $D(x,y,T_i) - T_V$ can only help the contour stop at target boundary MC_3. In Fig. 6.8a, the constant distribution of $D(x,y) - T_V$ using CODCM [1], though can stop the contour near MC_3, is inhomogeneous inside MC_3 and the contour has difficulties in marching over MC_1. Thus the method [1] fails to extract MC_3.

7. Parameter Setting Experiments

The proposed algorithm has over all ten parameters: T_V (Eq. (6)), a (Eq. (7)), b (Eq. (8)), threshold T_p (Eq. (22)), multipliers l_2 (Eq. (22)), l (iteration number per parameter updating in algorithm Step iv), velocity threshold V_t, maximum iteration number t_m, initial temperature T_{init}, and temperature updating factor $decT$. In the method, we do not need to tune T_p and l_2 since their setting does not affect solution. Velocity threshold V_t and maximum iteration number t_m are common parameters for level set algorithms [3] and in all the experiments, we keep V_t constant as 0.005 and t_m as 120. b is an implicit parameter of CODCM [1] and is set constant 2.0. l is related to the time step of every level set iteration and is set constant as 1. Thus in the method, there are four parameters, T_V, a, T_{init} and $decT$, need tuning. The setting of a is related to contour smoothness and is set large for boundaries with large gaps. In case of small or no large gap, a is often set as 0.01.

In the following, we will illustrate the experiments that evaluate the effects using different settings of T_V, T_{init}, and $decT$ on energy minimization. To facilitate the evaluations, we keep $a = 0.01$ unchanged and assume that $\overline{\Omega_C(t,T_i)} \subseteq \Omega_\Gamma$ is satisfied as the contour evolves. The first experiment is to evaluate the effect of the setting of T_V on constrained global energy minimization. We keep T_{init} as 10^7 and $DecT$ as 0.9 unchanged, then reduce the values of T_V and evaluate the energies of the resulting contours corresponding to different T_Vs. With smaller T_V, the region constraint is more relaxed and the resulting contours tend to have lower energy. Fig. 7.1a is a 256 by 256 synthetic image. The image is composed of four concentric circles, $CR_i, i = 1 \sim 4$, with their brightness radially distributed according to sine function and edges sharpened by four edge profile functions. The values of $D_{\min}(x,y)$, s^2, I_0 inside each of the circles and the respective contour energy E_C are listed in the following table,

	$D_{\min}(x,y)$	s^2	I_0	E_C
CR_1	0.395	917	214	0.0173
CR_2	0.158	744	203	0.0157
CR_3	0.044	636	192	0.0111
CR_4	0.0087	570	182	0.0098

Table 7.1 The parameters and energy for CR_1, CR_2, CR_3, and CR_4

In the experiment, the initial contour is set at the center of circles $CR_i, i = 1 \sim 4$ and we respectively choose T_V as 0.0001, 0.03, 0.1, and 0.35. The resulting contours CR_1, CR_2, CR_3, and CR_4 are shown in Fig. 7.1b to 7.1e. From the experiment, we can see that with a small $T_V = 0.0001$, CR_1, CR_2, CR_3, and CR_4 all satisfy the region constraint thus the contour with lowest energy is resulted. As the value of T_V increases, fewer contours satisfy the region constraint thus contours with higher energy are resulted as shown in Table 7.1.

The second experiment is to evaluate the effect of the settings of $decT$ and T_{init} on constrained global energy minimization. In the experiment, we keep $T_V = 0.001$ unchanged. The experiments are conducted in a 256 by 256 MRI brain image shown in Fig. 7.2a with the initial location I marked as a white dot shown in Fig. 7.2b. As we can see, in Fig. 7.2a, the interior of the intracranial is very inhomogeneous, where numerous local energy minima exist. Since $T_V = 0.001$ is small, most of the local energy minimum contours satisfy the region constraint of Eq. (10). By evaluating the energies of the resulting contours with different $decT$ and T_{init}, we will show that for a given value of $decT$ (or T_{init}), a higher T_{init} (or $decT$) is more capable of overcoming local energy minima and results lower contour energy while a lower T_{init} (or $decT$) indicates just the opposite.

To test the effect of the settings of T_{init}, we set $decT = 0.85$ and conduct the experiments by increasing the value of T_{init} from $T_{init} = 5*10^5$ to $T_{init} = 5*10^9$. The energies of the resulting contours with different settings of T_{init} are listed in Table 7.2. One can observe that increasing T_{init} has the effects of producing contours with lower contour energy. To test the effect of the settings of $decT$, we set $T_{init} = 5*10^6$ and conduct the experiments by increasing the value of $decT$ from 0.85 to 0.98 with the energies of the resulting contours listed in Table 7.3. One can also observe that increasing $decT$ has the effects of increasing the capability of overcoming local contour energy minima and resulting lower energy contour. The third experiment is to test the sensitivity of the algorithm to the positions of the initial contour. In order to quantify the sensitivity, we pick two extra initial points, initial point II and III, besides initial point I shown in Fig 7.2b and compute the average distance between the resulting contours using these initial contours. We take two measures to quantify the distances between different contours. The first distance measure is introduced in [27], which is written as $e_1 = 1 - \frac{|TP \cap EP|}{|TP \cup EP|}$ with TP denoting the set of pixels inside one of the resulting contour C_1 and EP denoting the set of pixels inside another resulting contour C_2. The measure e_1 is an indicator of the overall distance between the resulting contours. The second distance measure is $e_2 = \max_{X \in C_1} \min_{Y \in C_2} dist(X, Y)$ with $dist(X, Y)$ function representing the Euclidean distance between the integer coordinates of the pixels X and Y. e_2 is a local measure useful in determining the distance between the high curvature portions of the resulting contours. To test the sensitivity of e_1 and e_2 to T_{init}, we keep $decT$ unchanged at 0.85 and increase T_{init} from $5*10^6$ to $5*10^8$. To test the sensitivity to $decT$, we keep T_{init} unchanged at $5*10^6$ and increase $decT$ from 0.85 to 0.98. The computed average distances are listed in Table 7.4. As we can see from the data, the algorithm becomes to be more sensitive when T_{init} and $decT$ increase and vice versa.

Table 7.1

	$T_{init} = 5*10^5$	$T_{init} = 5*10^6$	$T_{init} = 5*10^7$	$T_{init} = 5*10^8$	$T_{init} = 5*10^9$
Contour Energy	0.04144	0.030626	0.030192	0.024595	0.0185531

Table 7.2

	$DecT = 0.85$	$DecT = 0.92$	$DecT = 0.94$	$DecT = 0.96$	$DecT = 0.98$
Contour Energy	0.030626	0.0299965	0.0251968	0.0163892	0.0141091

Table 7.3

	e_1	e_2
$T_{init} = 5*10^6, DecT = 0.85$	0.1195	5.886
$T_{init} = 5*10^7, DecT = 0.85$	0.1505	9.025
$T_{init} = 5*10^8, DecT = 0.85$	0.1725	22.923
$T_{init} = 5*10^6, DecT = 0.94$	0.1295	18.669
$T_{init} = 5*10^6, DecT = 0.98$	0.134	20.695

8. Applications

Our experimental evaluations and comparisons can be divided into three separate items and we separately discuss each category as follows:

i) Contour evaluations are performed on a set of challenging contour extraction problems including ultrasound pig heart images having noisy contour interiors, sharp contour segment protrusions, and gaps as shown in Fig. 8.1, MRI knee images having thick and very blur contour segment and contour-within-contour segment as shown in Fig. 8.2, and MRI brain images having contours with complex shape, inhomogeneous interiors, and blur segments as shown in Figs. 8.3, 8.4, and 8.5. All resulting contours are shown on the right-hand side of their originals in Figs. 8.1, 8.2, 8.4 and 8.5. Notice that for the MRI brain images, we perform three separate extractions of external boundary of intracranial (Fig. 8.3), cerebral boundary (Fig. 8.4), and sulci boundary (Fig. 8.5). Furthermore, Fig. 8.3 shows a sequence of contour progression images. All these contours are considered very good results.

ii) A performance comparison between the proposed method and CODCM [16] is made on four images shown in Figs. 8.6 (a), 8.6(b), 8.7(a), and 8.8(a) of visual blood cell image, MRI knee image, and two MRI brain images respectively. In Fig. 8.6(a), the cells have rather large gaps and in Fig. 8.6(b), there are blur boundary segment and a rather inhomogeneous interior. In Fig. 8.7(a) and 8.8(a), there are very inhomogeneous interiors inside the external boundaries of intracranial. As we see from the results shown in Fig. 8.6(c) to 8.6(f), 8.7(b), 8.7(c), 8.8(b), 8.8(c), comparing to the result of [16], substantial improvements can be seen.

iii) The proposed method is also compared to other conventional deformable contour methods; the first two methods are geodesic snake [4], and area & length active contour [10] using $h(x,y)=\frac{1}{1+|\nabla G*I|^2}$ as the edge detection function and the third method is T-snake [11]. We select two zoomed images of Fig. 8.9a a stomach CT image with additive noise of Gaussian noise (variance 3000), and Fig. 8.10a a midline sagittal MRI brain image. Similar to all other three methods, a Gaussian filter $N(0, 1)$ is applied to both images as a preprocessing operation. No a priori information of object shape or brightness distribution is assumed (that is why [6][7][8] are not included). To provide an objective comparison, two sets of three dark dots in Fig. 8.9a and Fig. 8.10a are used as initial candidate locations for all four methods including ours. Each method using an initial candidate location provides a resulting contour. The best contour (best of the three resulting contours for Fig. 8.9a and Fig. 8.10a) of each method from all initial candidate locations is selected for comparison. Comparing these resulting contours, our proposed method has the best contours. It should be noted that similar comparisons have been conducted in [16] and a thorough comparison with quantitative analysis may be found in [28].

9. Conclusions

In this paper, a constrained global optimization formulation has been proposed for boundary extraction problems. The formulation overcomes the problems of multiple local energy minima while preserves good controllability in extracting target boundaries with different region characteristics. The effectiveness of the approach in locating constrained global energy minima is evaluated in a synthetic test image, where constrained global energy minima are known. The results are compared to those of CODCM [1] with the same energy function and region constraint, where an accurate estimation of the object interior features is assumed. ***The experiment proves that the contribution of the method can not be reduced as only providing a dynamic parameter estimation to avoid manual parameter tuning.*** The performance of the method is then demonstrated on very challenging segmentation applications and is compared to those of other deformable contour methods and substantial improvements in handling segmentation difficulties including gaps, noises, and blur boundaries are reported. The method is computationally efficient usually taking 10 seconds to 2 minutes on workstation Ultra Sun Blade 100 for most applications.

Appendix

Noting that in Eq. (22) $l_1^* << l_2$ and $L_p \approx E_{II}$, $\overline{I_0(T_i)}$ can be computed as

$$\overline{I_0(T_i)} = \frac{\int_{-\infty}^{\infty} I_0 e^{-L_p(I_0)} dI_0}{\int_{-\infty}^{\infty} e^{-L_p(I_0)} dI_0} \approx \frac{\int_{-\infty}^{\infty} I_0 e^{-E_{II}(I_0)} dI_0}{\int_{-\infty}^{\infty} e^{-E_{II}(I_0)} dI_0} = I_0^C(T_i)\,.$$

In the following, we compute $s^2(T_i)$ and $l_1^*(T_i)$. We assume that $\overline{\Omega_C(t,T_1)} \subseteq \Omega_\Gamma$, where $\overline{\Omega_C(t,T_1)}$ is the interior of $\overline{C(q,t,T_1)}$. Noting that $C(q,0,T_1)$ is a 5 by 5 contour inside target boundary $\Gamma(q)$, the condition can be easily satisfied in most applications. Let $i = 1$. $s^2(T_i)$ should satisfy

$$\min D(x,y) = \min \exp\left(-\frac{(I(x,y)-I_0)^2}{b s^2(T_i)}\right) \geq T_V \qquad \text{for } (x,y) \in \overline{\Omega_C(t,T_i)}$$

Let s_o^2 satisfy
$$\min \exp\left(-\frac{(I(x,y)-I_0)^2}{b s_o^2}\right) = T_V \qquad \text{for } (x,y) \in \overline{\Omega_C(t,T_i)}$$

It is obvious that $s^2(T_i) \geq s_o^2$. Since the computation of $s^2(T_i)$ based on s_o^2 is rather complex, in implementations, we approximate s_o^2 by $s_C^2(T_i)$ and compute $s^2(T_i)$ as,

$$\overline{s^2(T_i)} = \frac{\int_{s_C^2}^{\infty} s^2 e^{-L_p(s^2)} ds^2}{\int_{s_C^2}^{\infty} e^{-L_p(s^2)} ds^2} \approx \frac{\int_{s_C^2}^{\infty} s^2 e^{-E_{II}(s^2)} ds^2}{\int_{s_C^2}^{\infty} e^{-E_{II}(s^2)} ds^2} = s_C^2(T_i) + \sqrt{\frac{T_i}{p}} \qquad \text{(A-1)}$$

Similarly, the estimated value of $l_1^*(T_i)$ has to satisfy

$$\min\left(\frac{\partial \overline{C(q,t,T_i)}}{\partial t}\right) = \min\left[\left\{l_1^*(T_i)\left[D(x,y,T_i) - T_V\right] + kg(|\nabla I|) - \nabla g \cdot \vec{N}\right\}\vec{N}\right] \ge 0 \qquad \text{for } (x,y) \in \overline{C(q,t,T_i)}$$

Let l_1^o be $\quad \min\left[\left\{l_1^o\left[D(x,y,T_i) - T_V\right] + kg(|\nabla I|) - \nabla g \cdot \vec{N}\right\}\vec{N}\right] = 0 \qquad \text{for } (x,y) \in \overline{C(q,t,T_i)}$

Then we have $l_1^*(T_i) \ge \max(l_1^o, 0)$. To simplify computations, we approximate $\max(l_1^o, 0)$ by $l_1^C(T_i)$ and thus have

$$\overline{l_1^*(T_i)} = \frac{\int_{l_1^C}^{\infty} l_1^* \exp\left\{-\frac{(l_1^* - l_1^C)^2}{T_i}\right\} dl}{\int_{l_1^C}^{\infty} \exp\left(-\frac{(l_1^* - l_1^C)^2}{T_i}\right) dl} = l_1^C(T_i) + \sqrt{\frac{T_i}{p}} \qquad \text{(A-2)}$$

From Eq. (A-1) and (A-2), it is obvious that $\overline{s^2(T_i)} \ge s_C^2(T_i)$, $\overline{l_1^*(T_i)} \ge l_1^C(T_i)$. Let $s_C^2(T_0) = s^2_{C(q,0,T_1)}$, $l_1^C(T_0) = l_1^{C(q,0,T_1)}$, and $I_0^C(T_0) = I_0^{C(q,0,T_1)}$. Please be noted that T_0 does not exist and the above equations only serve to simplify notations for the following discussions. Since the contour deformations made in Step1 are small, the differences between $s_C^2(T_i)$ and $s_C^2(T_{i-1})$, $l_1^C(T_i)$ and $l_1^C(T_{i-1})$ can be ignored. In Eq. (A-1) and (A-2), as $T_i \to 0$, $\overline{l_1^*(T_i)} \to l_1^C(T_i) \approx l_1^C(T_{i-1})$, $\overline{s^2(T_i)} \to s_C^2(T_i) \approx s_C^2(T_{i-1})$, $\overline{I_0(T_i)} = I_0^C(T_i) \approx I_0^C(T_{i-1})$, $\overline{C(q,t,T_{i+1})}$ computed according to Eq. (24) either will stop at $\overline{C(q,t,T_i)}$ (for $i=1$) or may even move backward (for $i>1$) therefore $\overline{\Omega_C(t,T_{i+1})} \subseteq \Omega_\Gamma$ is guaranteed to be satisfied. By a careful selection of T_i, $\overline{C(q,t,T_{i+1})}$ can move outward and approach target boundary while satisfy $\overline{\Omega_C(t,T_{i+1})} \subseteq \Omega_\Gamma$. With $\overline{\Omega_C(t,T_{i+1})} \subseteq \Omega_\Gamma$, we can then repeat the above procedures for computing $\overline{l_1^*(T_{i+1})}$, $\overline{s^2(T_{i+1})}$, $\overline{I_0(T_{i+1})}$ and let $i = i + 1$ until i equals n.

Reference

[1] X. Wang, L. He, and W. Wee, "Constrained Optimization: A Geodesic Snake Approach", vol. II, pp.77-80, IEEE ICIP, 2002

[2] M. Kass, A. Witkin and D. Terzopoulos, Snakes: Active Contour Models, *IJCV,* 1 (4) pp. 321-331, 1998.

[3] R. Malladi, J. Sethian and B. Vemuri, Shape Modeling with Front Propagation, *IEEE Trans on PAMI*, 17 (2) pp. 158-171, 1995.

[4] V. Casellas, R. Kimmel and G. Sapiro, Geodesic Active Contours, *IJCV*, 22 (1) pp. 61-79, 1997.

[5] X. Wang, L. He, and W. Wee, "A Constrained Optimization Approach to Deformable Contour Method", pp. 183-192, British Machine Vision Conference, 2002.

[6] T. Chan and L. Vese, Active Contours without Edges, *IEEE Trans on Image Processing*, 10 (2) pp. 266-277, 2001.

[7] C. Samson, L. Blanc-Feraud, G. Aubert and J. Zerubia, A Level Set Model for Image Classification, *IJCV,* 40 (3) 187-197, 2000.

[8] N. Paragios and R. Deriche, Geodesic Active Contours and Level Set Methods for Supervised Texture Segmentation, *IJCV*, Mar. 2002.

[9] D. Geiger, Girosi, F., Parallel and deterministic algorithms from MRFs: surface reconstruction *IEEE Trans. on PAMI*, 13 (5), pp. 401 – 412, 1991.

[10] K. Siddiqi, Y. B. Lauziere, A. Tannenbaum, S. W. Zucker, Area and length minimizing flows for shape segmentation, *IEEE Trans. on Image Processing,* Vol. 7 pp 433-443, 1998.

[11] T. McInerney and D. Terzopoulos, Topology adaptive deformable surfaces for medical image volume segmentation. *IEEE Trans. on Medical Imaging*, Vol. 18, No.10, pp. 840-850, 1999.

[12] C. Xu, and J. Prince, Snakes, shape, and gradient vector flow. *IEEE Trans. on Image Processing*, Vol. 7, pp. 359-369, 1998.

[13] L. Cohen, On active contour models and balloons, *CVGIP: Image Understanding*. Vol. 52, No.2, pp. 211-218, March, 1991.

[14] Stovik, G. 1994. "A Bayesian approach to dynamic contours through stochastic sampling and simulated annealing". *IEEE Trans. on PAMI*, Vol.16, No.10, pp. 976-986.

[15] Grzeszczuk, R. and Levin, D. 1997. ""Brownian String", Segmenting images with stochastically deformable contours". *IEEE Trans. on PAMI*, Vol. 19, No. 10, pp. 1100-1114.

[16] X. Wang, L. He, and William G. Wee, "A Constrained Optimization Approach to Deformable Contour Method", *IJCV* (in press) (can also be found in www.ececs.uc.edu/~xwang)

[17] Tsai A, Zhang J, Willsky A, "Expectation-Maximization Algorithms for Image Processing Using Multiscale Methods and Mean Field Theory, with Applications to Laser Radar Range Profiling and Segmentation", Optical Engineering, vol. 40, no. 7, pp. 1287-1301, July 2001.

[18] N. Paragios and M. Rousson, "Shape Priors for Level Set Representations", Proceedings of European Conference in Computer Vision, (ECCV 2002) June 2002.

[19] D. Cremers, T. Kohlberger, and C. Schnorr, "Nonlinear Shape Statistics in Mumford-Shah Based Segmentation," pp. 93-109, ECCV 2002.

[20] X. Wang, F. Gao, Z. Peng, L. He, and W. Wee, "An Integrated Approach to the Segmentation and Recognition of Objects using Thin Plate Spline Method", International Conference of Vision Interfaces 2003.

[21] T. Hofmann, J. Puzicha, J. M., Buhmann, "Unsupervised texture segmentation in a deterministic annealing framework", IEEE Trans on PAMI, pp. 803-818, Vol. 20 No. 8 , Aug. 1998.

[22] Yuri Boykov, Olga Veksler and Ramin Zabih, "Fast Approximate Energy Minimization via Graph Cuts", IEEE Trans. on PAMI, Vol. 23, No. 11, Nov. 2001.

[23] S. Geman and D. Geman, "Stochastic Relaxation, Gibbs Distribution, and the Bayesian Restoration of Images", IEEE Trans. on PAMI, Vol. 6, pp 721 – 741, 1984.

[24] D. Greig, B. Porteous, and A. Seheult, "Exact Maximum: A Posteriori Estimation for Binary Images," J. Royal Statistical Soc., Series B, Vol. 51, No. 2, pp. 271-279, 1989.

[25] Yuri Boykov and Marie-Pierre Jolly, "Interactive Graph Cuts for Optimal Boundary and Region Segmentation of Objects in N-D images", ICCV, Pages I: 105-112, 2001.

[26] T. Hofmann and J. M. Buhmann, "Pairwise data clustering by deterministic annealing", IEEE Transactions on PAMI, Vol. 19, No. 1, pp 1- 14, Jan. 1997.

[27] J. Tohka, "Surface extraction from volumetric images using deformable meshes: a comparative study," *the seventh European Conference on Computer Vision*, pp. 350-364, 2002.

[28] L. He, B. Everding, Z. Peng, X. Wang, C.Y. Han, K. Weiss, and W.G.Wee, "A Comparative Survey of Deformable Contour Methods on Medical Image Segmentation", IEEE Trans. on Medical Imaging, (under second round review).

[29] A. Daniilidis and C. Lemarechal, "Proximal Convexification Procedures in Combinatorial Optimization", INRIA Research Report RR 4550, September 2002.

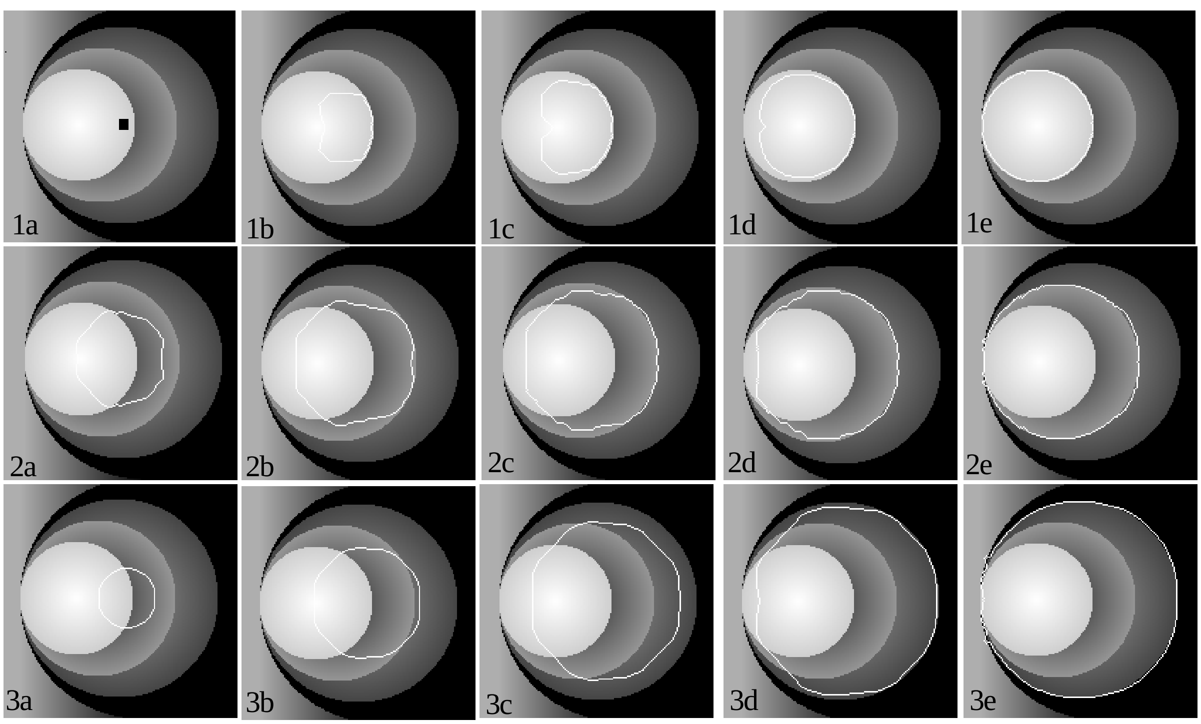

Fig. 6.1b to 6.1e illustrate the contour evolution process of extracting MC_1 using the proposed method. Fig. 6.2a to 6.2e, and Fig. 6.3a to 6.3e illustrate the contour evolution process of extracting MC_2 and MC_3 respectively using the proposed method

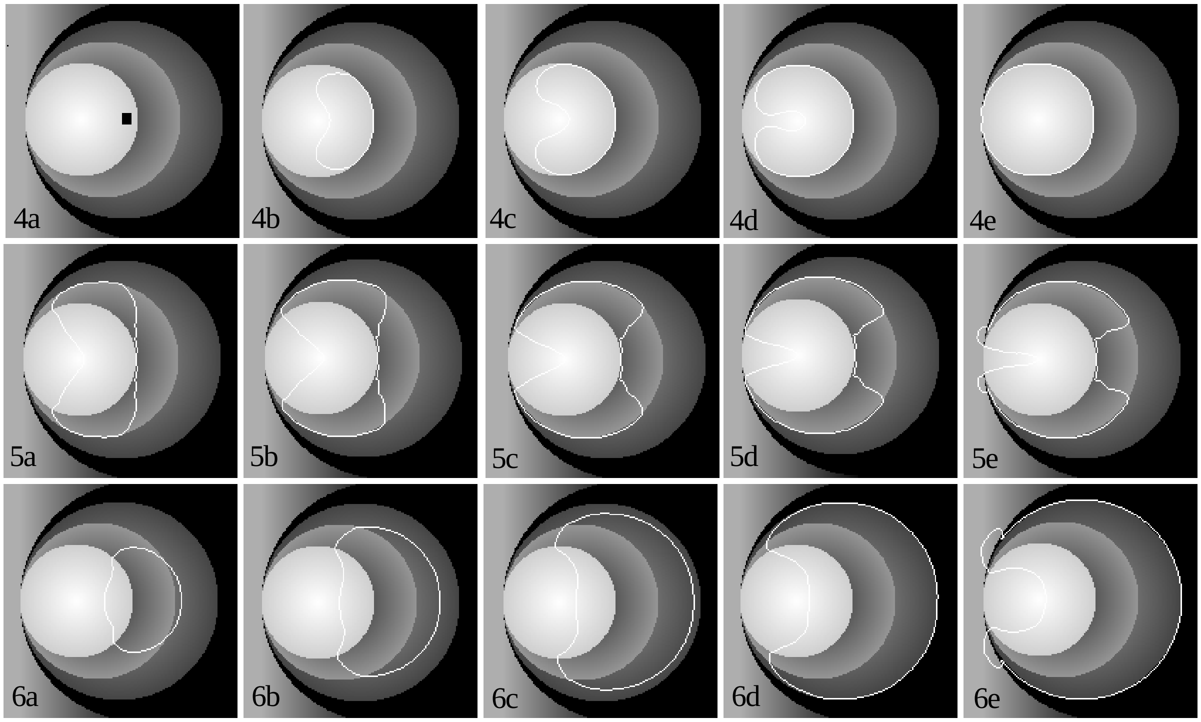

Fig. 6.4b to 6.4e illustrate the contour evolution process of extracting MC_1 using Eq. (17). Fig. 6.5a to 6.5e, and Fig. 6.6a to 6.6e illustrate the contour evolution process of extracting MC_2 and MC_3 respectively using Eq. (17)

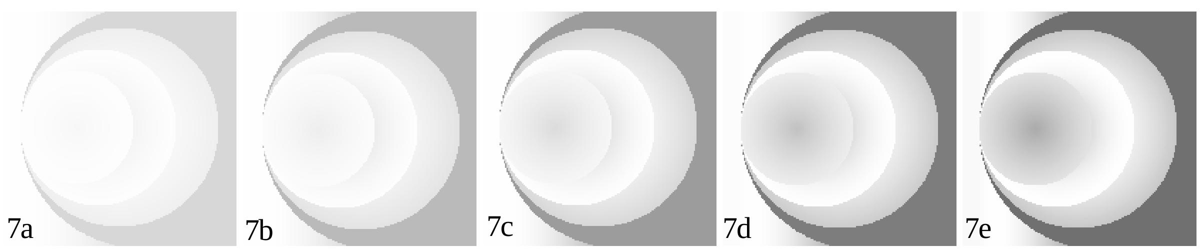

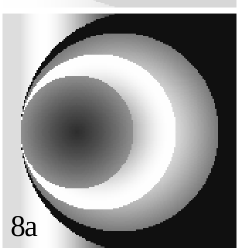

Fig. 6.7a to 6.7e illustrate the scaled image of $D(x, y, T_i) - T_V$ in Eq. (24) under the temperatures corresponding to Fig. 6.3a to 6.3e respectively. Fig. 6.8a illustrates the scaled image of $D(x, y) - T_V$ in Eq. (17).

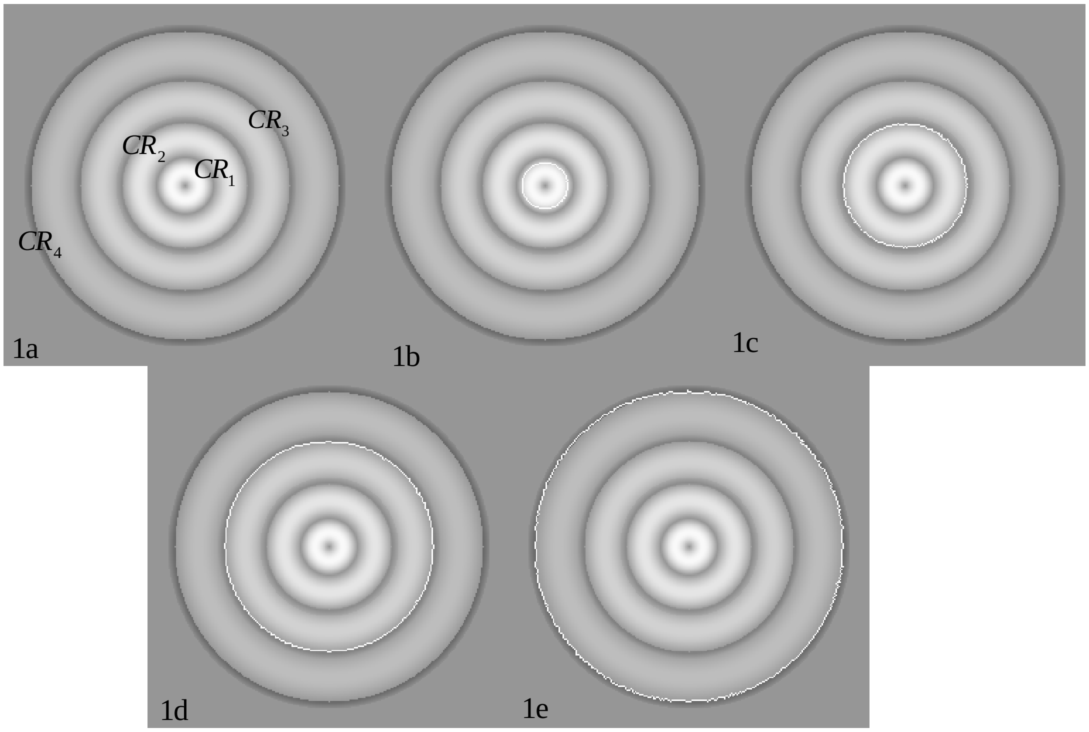

Fig. 7.1a The test image for different settings of T_V. Fig. 7.1b The resulting contour with $T_V = 0.35$, Fig. 7.1c The resulting contour with $T_V = 0.1$, Fig. 7.1d The resulting contour with $T_V = 0.03$, Fig. 7.1e The resulting contour with $T_V = 0.0001$.

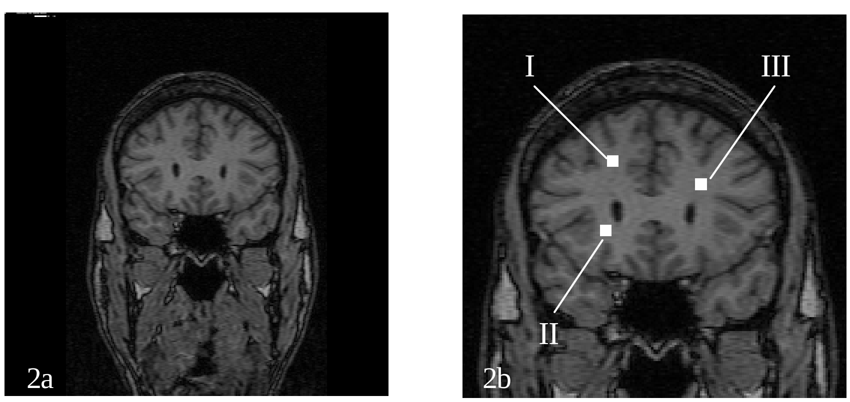

Fig. 7.2a Test image for parameter sensitivity experiments. Fig. 7.2b Zoomed image of the brain and the positions of the initial locations I, II, and III.

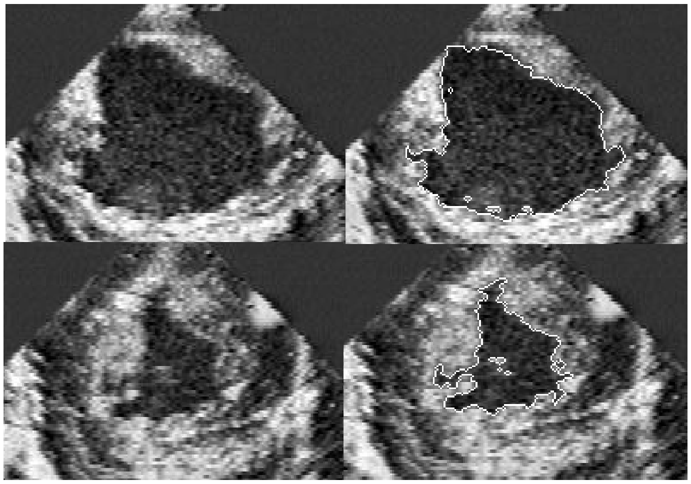

Fig. 8.1 Ultrasound pig heart original images in the left column and their corresponding results in the right column

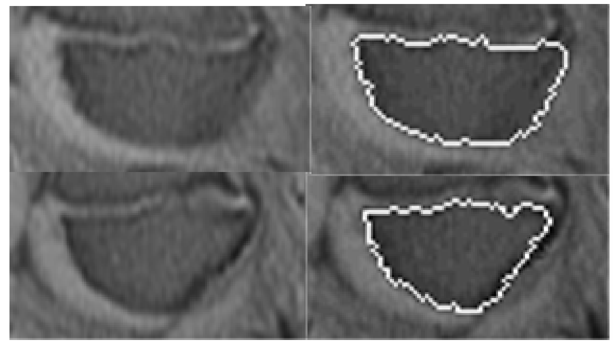

Fig. 8.2 MRI knee original images on the left column and their corresponding results on the right column

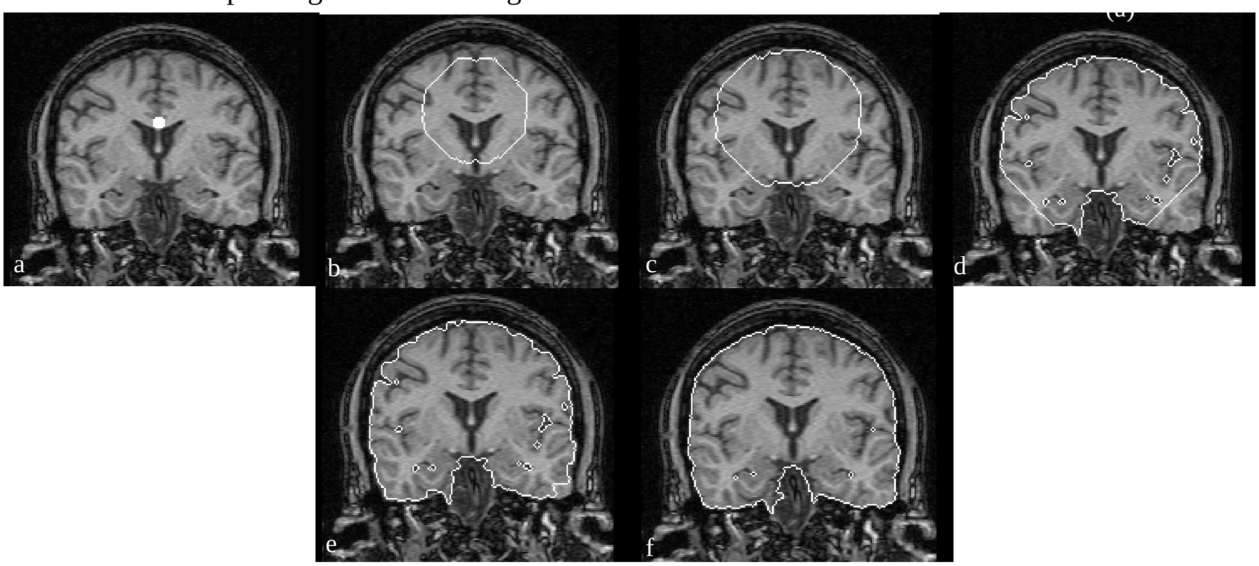

Fig. 8.3 (a) Original MRI brain mage (white dot indicates the position of the initial contour). (b) to (g) The extraction process of the exterior boundary of intracranial

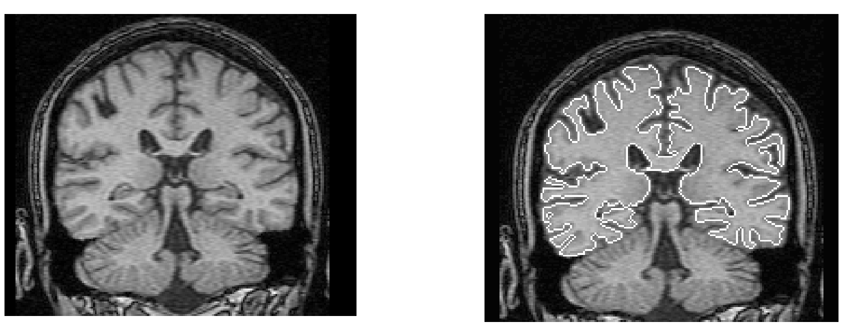

Fig. 8.4 MRI brain image two and the result

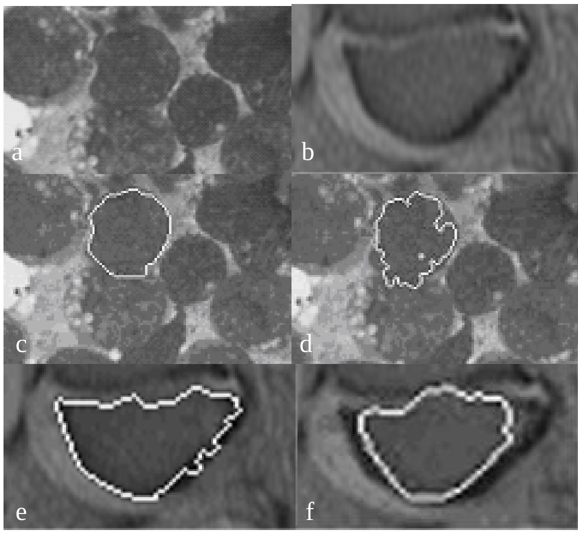

Fig. 8.6 Comparison results with CODCM [16]. (c) and (e) are segmentation results using the proposed method. (d) and (f) are segmentation results using CODCM [16].

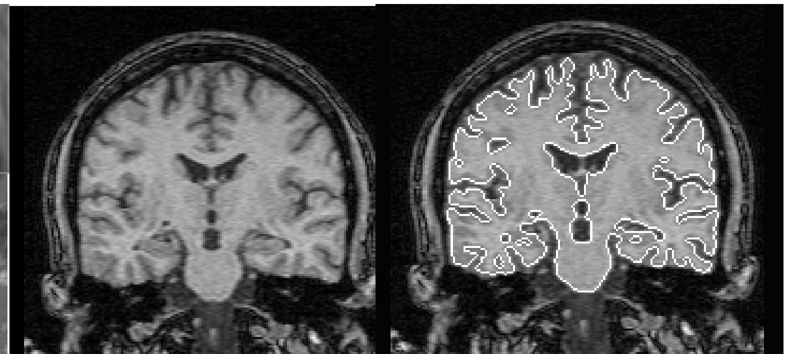

Fig. 8.5 MRI brain image three and the result

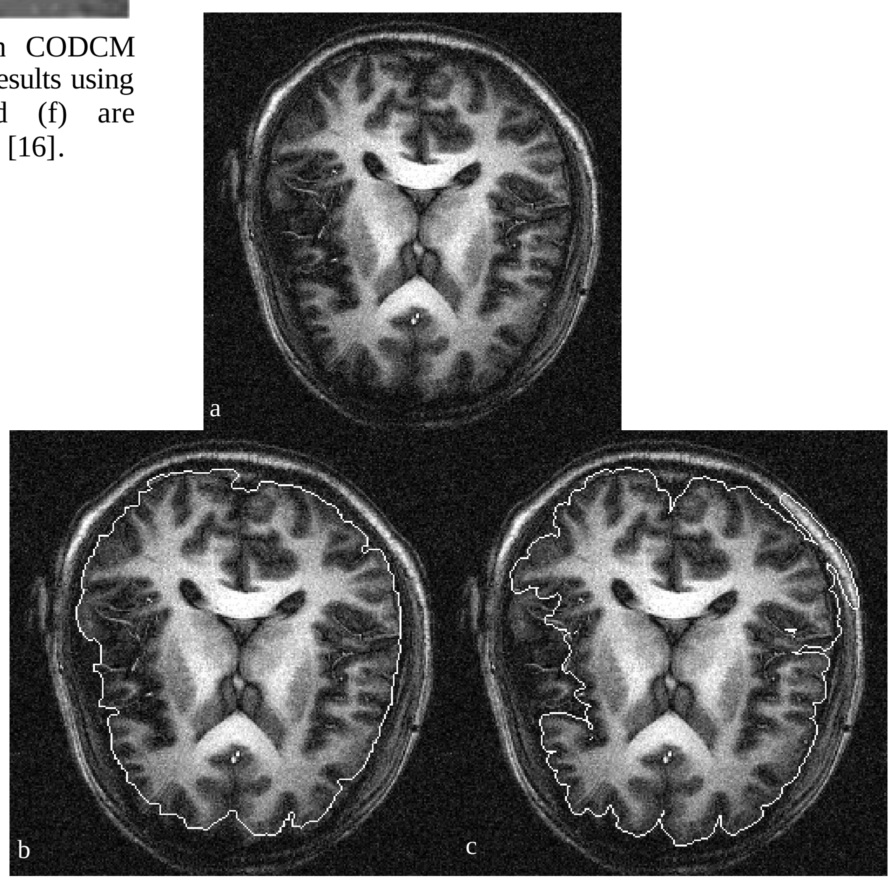

Fig. 8.7 Comparison results with CODCM [16]. (b) is the segmentation result of the external boundary of intracranial using the proposed method. (c) is the segmentation result of the external boundary of intracranial using CODCM [16].

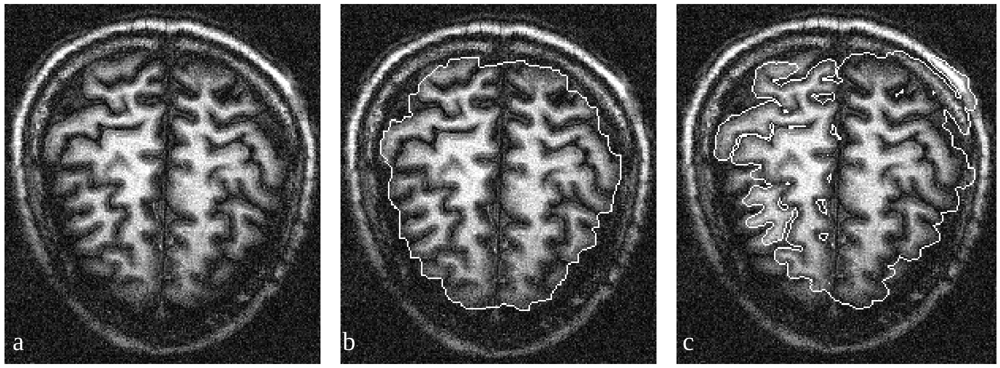

Fig. 8.8 Comparison results with CODCM [16]. (b) is the segmentation result of the external boundary of intracranial using the proposed method. (c) is the segmentation result of the external boundary of intracranial using CODCM [16].

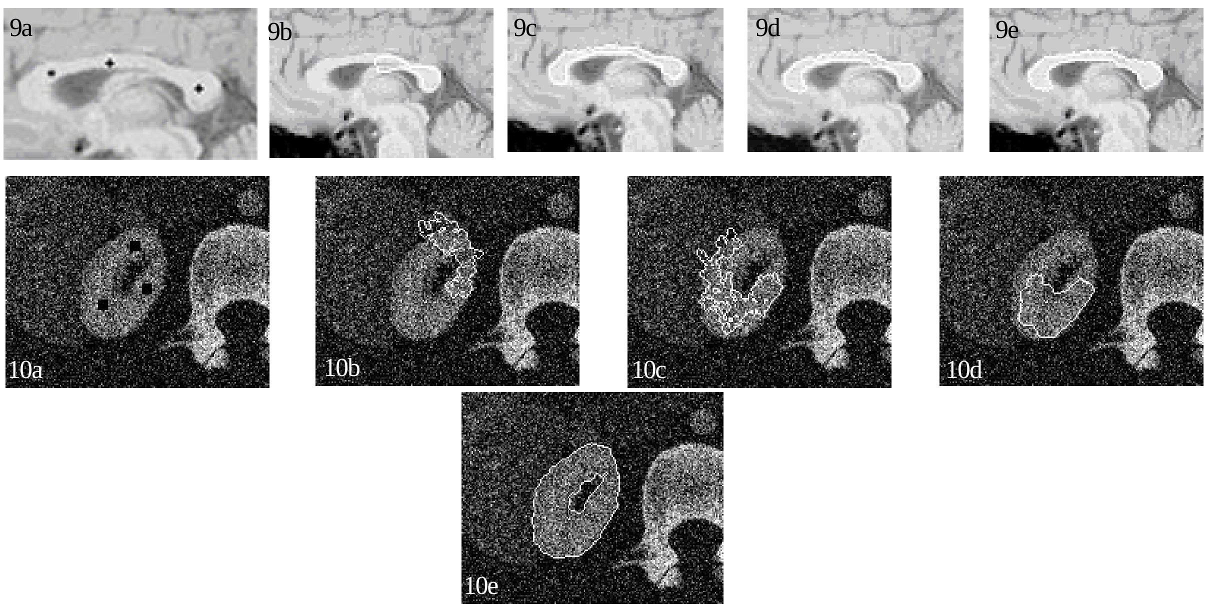

Fig. 8.9a, 10a Original images of the comparison, 9b, 10b The results of T-snake, 9c, 10c The results of geodesic snake, 9d, 10d The results of Area-length snake, 9e, 10e The results of proposed method.